JGR Solid Earth

Coseismic and Postseismic Deformation of the 2016 Central Tottori Earthquake and its Slip Model

Angela Meneses-Gutierrez[1] (iD) **, Takuya Nishimura[1]** (iD) **, and Manabu Hashimoto[1]** (iD)

[1]Disaster Prevention Research Institute, Kyoto University, Kyoto, Japan

Abstract We analyze Global Navigation Satellite System (GNSS), Interferometric Synthetic Aperture Radar, and accelerometer data within the San-in Shear Zone in order to clarify the coseismic and postseismic slip distributions associated with the M_w6.2 2016 Central Tottori earthquake. Inversion of the coseismic displacement data to estimate the slip distribution on the rupture fault shows a patch of large slip to the northwest of the hypocenter of the mainshock location. Relocated aftershocks and off-fault seismicity 1 month after the mainshock are in agreement with stress change patterns caused by the mainshock fault. Inversion of near-field GNSS displacements in 7 months following the earthquake under the assumption of afterslip does not show a preferred slip patch but rather a smooth distribution of the slip at shallow depths. Restricted slip propagation of afterslip on the 2016 event might suggest that inland faults in the San-in Shear Zone are immature. Limited resolution of the GNSS data might inhibit us from finding the slip at depth.

1. Introduction

The San-in Shear Zone (SSZ) is an ~N80°E right-lateral shear zone in southwestern Japan with a 30- to 50-km width, where high seismicity and high strain rates have been observed (Nishimura & Takada, 2017). Historically, numerous earthquakes have occurred in this deformation zone. In the past century several large earthquakes have occurred within the SSZ, such as the 1943 Tottori earthquake (M_j 7.2; e.g., Kanamori, 1972), the 1983 Central Tottori earthquake (M_j 6.2; e.g., Oike, 1987), and the 2000 Western Tottori earthquake (M_j 7.3; e.g., Ohmi et al., 2002; Figure 1), showing that the SSZ is seismotectonically active. Recent seismic events, excluding the 1943 earthquake, exhibit left-lateral motion on NNW-SSE oriented faults, despite the general right-lateral motion observed on the SSZ. Such behavior has been interpreted as conjugate Riedel shears in a shear zone (Nishimura & Takada, 2017).

On 21 October 2016 a M_j 6.6 left-lateral strike-slip fault-type earthquake occurred in the central part of the Tottori prefecture, within the SSZ (Figure 1). The occurrence of this earthquake (hereafter the 2016 Central Tottori earthquake) considerably affected the crustal deformation pattern in the area. Strong ground acceleration in the nearby region was reported by the National Research Institute for Earth Science and Disaster Resilience (NIED), and crustal movements associated with this event were recorded by the nationwide Global Navigation Satellite System (GNSS) Earth Observation Network System (GEONET) operated by the Geospatial Information Authority of Japan.

GEONET is composed of over 1,300 GNSS stations distributed across Japan. This network has allowed the identification of deformation processes during the different stages of the earthquake cycle (e.g., Sagiya, 2004). Nevertheless, the average distance between GEONET sites (~20 km) is still not short enough to detect small rate changes associated with shallow inland faulting in Japan, as well as detailed deformation patterns in the postseismic period of earthquakes with moderate magnitude (M < ~6.5). Thus, densification of GNSS networks is fundamental to study crustal processes.

In an effort to better characterize deformation within the SSZ, our research group constructed 13 continuous GNSS sites in and around the Tottori prefecture in 2014 (Figure 1). These stations recorded near-field coseismic and postseismic deformation of the 2016 Central Tottori earthquake. Additionally, two stations were deployed a month after the earthquake to monitor postseismic deformation in the area. Analysis of these data in combination with GEONET data, available Interferometric Synthetic Aperture Radar (InSAR) images, and strong motion data can help to clarify the crustal deformation associated with the 2016 Central Tottori earthquake.

In this study, we analyze coseismic and postseismic deformation of the 2016 Central Tottori earthquake. To date, two coseismic slip distributions based on seismic data have been published for this event (Kubo et al.,
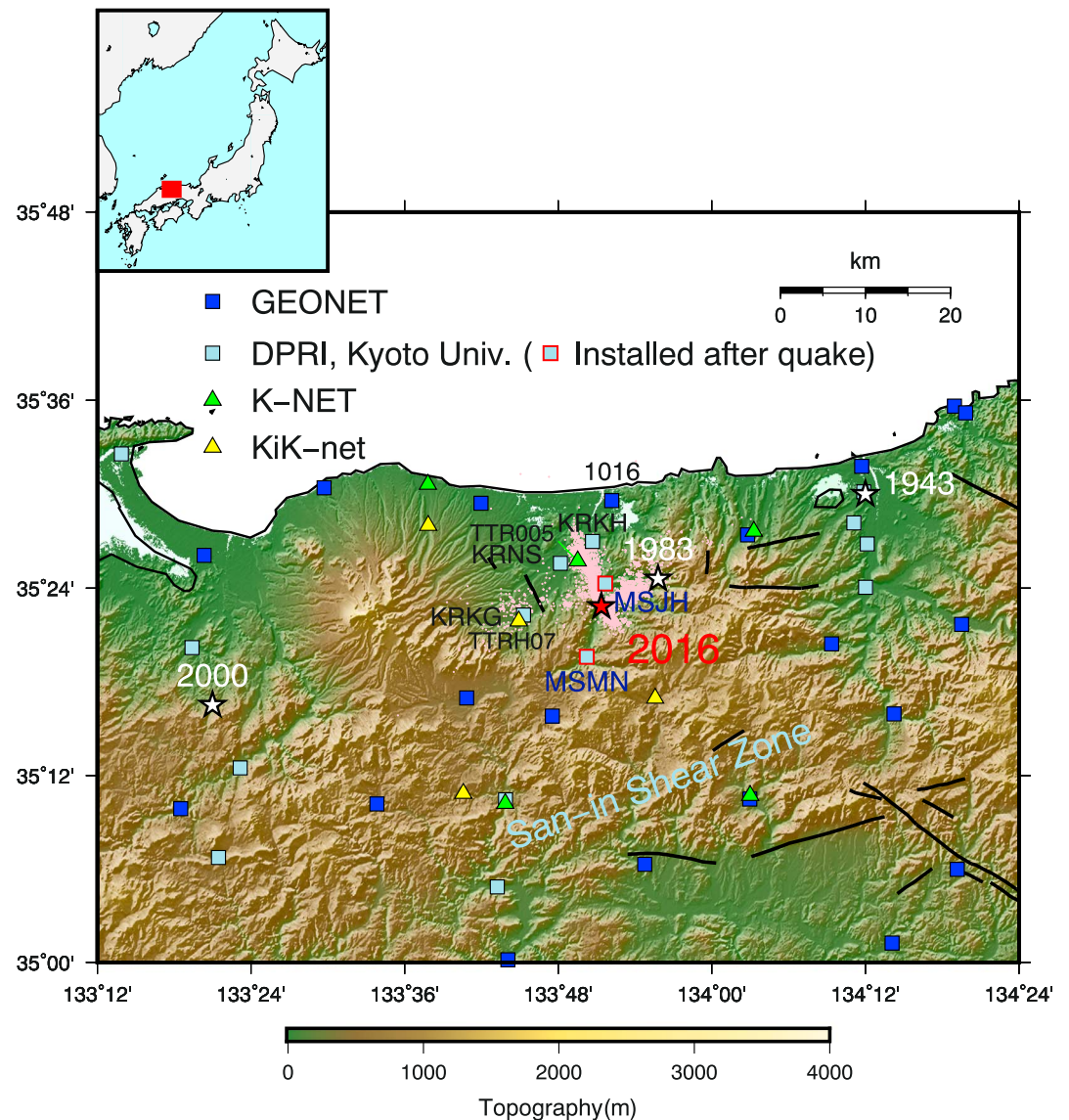
Figure 1. Topographical map showing GNSS and accelerometer data (K-NET and KiK-net) used for this analysis. White stars denote hypocenter location of the 1943 Tottori earthquake (*Mj* 7.2), the 1983 Central Tottori earthquake (*Mj* 6.2), and the 2000 Western Tottori earthquake (*Mj* 7.3), and red star denotes the 2016 Central Tottori earthquake. Thin black lines denote active Quaternary fault traces (Research Group for Active Faults of Japan, 1991). Topography data are taken from the Shuttle Radar Topography Mission digital elevation model (Jarvis et al., 2008). Aftershock distribution 1 month after the earthquake is shown by pink dots (Iio et al., 2018). Time series of selected stations are shown on Figures 2 and 4. Inset figure shows location with respect to the Japanese Islands.

2017; Ross et al., 2018). Kubo et al. (2017) analyzed near-field strong motion data using a multiple time window linear kinematic waveform inversion. They calculated Green's functions with the discrete wavenumber method in a 1-D layered velocity structure model and delimited two areas of concentrated slip on the fault plane and maximum slip of 0.6 m. On the other hand, Ross et al. (2018) inverted near- and far-field strong motion data using an empirical Green's function method. Their results indicate slip at depths, with large slip (~3.2 m) concentrated within a 3-km × 3-km area below 8-km depth. The models obtained by Kubo et al. (2017) and Ross et al. (2018) are different both in the magnitude and spatial distribution of the coseismic slip of the 2016 Central Tottori earthquake, indicating that one or both of the results are biased. Consequently, we construct the coseismic slip model for the 2016 Central Tottori earthquake based on available near-field seismic and geodetic data. Using a detailed deformation

field mapped by InSAR and GNSS has an advantage to resolve absolute location of shallow slip. We also provide a detailed description of the mechanism driving postseismic deformation, by taking advantage of the highly dense GNSS network in the area.

In the following, we first introduce a description of the used data sets. We then present the methodology employed to estimate detailed slip distributions during the coseismic and the postseismic periods. We finally discuss the implications of our results and its relationship to the seismotectonics in the area.

2. Data and Methodology

2.1. GNSS Data

We analyze data from 33 continuous GNSS sites in the vicinity of the 2016 Central Tottori earthquake. The network consists of 18 GEONET sites and 15 additional sites constructed by DPRI, Kyoto University to monitor crustal deformation in the SSZ (Figure 1). Thirteen stations were constructed in 2014 and 2 additional stations were deployed a month after the 2016 Central Tottori earthquake to monitor postseismic deformation of this event. Precise daily coordinates for the GNSS sites are calculated with the GNSS-Inferred Positioning System and Orbit Analysis Simulation Software, version 6.2 using the Precise Point Positioning processing strategy with ambiguity resolution (Bertiger et al., 2010; Zumberge et al., 1997). Precise satellite orbits, Earth orientation parameters, and satellite clock corrections were obtained from the final solutions provided by the Jet Propulsion Laboratory.

Daily coordinates time series indicate clear coseismic and postseismic transient deformation due to the 2016 Central Tottori earthquake (Figure 2). Postseismic deformation rapidly decays after the earthquake. Before the event steady motion with linear trend is recognized. Postseismic displacement is restricted to stations near to the source region of the event.

We calculate coseismic and postseismic displacements of the 2016 Central Tottori earthquake from the GNSS data as follows. At first, we estimate interseismic velocities for each coordinate time series from September 2014 to September 2016 by a combination of a linear trend and annual and semiannual sinusoidal variations, and then we proceed to remove them of the GNSS position time series from September 2014 to June 2017. To improve the precision of estimated displacements in our detrended time series, we apply a spatial filter to remove common mode errors in the data (Wdowinski et al., 1997; Figure 2). Interseismic horizontal velocities at stations installed after the 2016 Central Tottori earthquake are interpolated from the neighboring GNSS stations using the method developed by Shen et al. (1996). In this method, a distance decay constant (DDC) is applied to control the weight among the observation. Spacing between the GNSS sites in the SSZ in the interseismic period is ~20 km; thus, we use a DDC of 15 km as a standard value. Stations within 3 DDC from the calculation point are used for the estimation.

Coseismic and postseismic displacement are estimated by fitting the following function to each detrended daily coordinate for each station

$$u(t) = a + bH(t-t_{\text{eq}}) + cH(t-t_{\text{eq}}) \ln\left(1 + \frac{t-t_{\text{eq}}}{t_{DC}}\right) \tag{1}$$

Here the first term on the right side corresponds to the residual offset from the interseismic period, the next term is the coseismic displacement associated with the 2016 Central Tottori earthquake, and the last term indicates to the postseismic displacement. We assume that the postseismic displacement evolves logarithmically with time as expected by frictional afterslip (Marone et al., 1991). H represent the Heaviside function, t_{eq} denotes the time of the earthquake, and t_{DC} is the time decay constant for the postseismic deformation.

We use 7 months of daily coordinates after the 2016 Central Tottori earthquake to study postseismic deformation. We assume that the spatial pattern of afterslip distribution does not change with time and constrain the appropriate time decay constant to describe the postseismic deformation in the area by considering only the closest stations to the source region which displayed the largest postseismic slip (stations KRKG, KRNS, KRKH, and 1016 in Figure 1). We apply a nonlinear least squares method and determined the time decay constant according to the minimum root mean square value in comparison with the observation. We tested values from 0 to 60 days every 0.1 days and found that for a data period of 210 days, time decay constant of 2.2 days describes the observations in the near field best (Figure 2). This value is within the range of
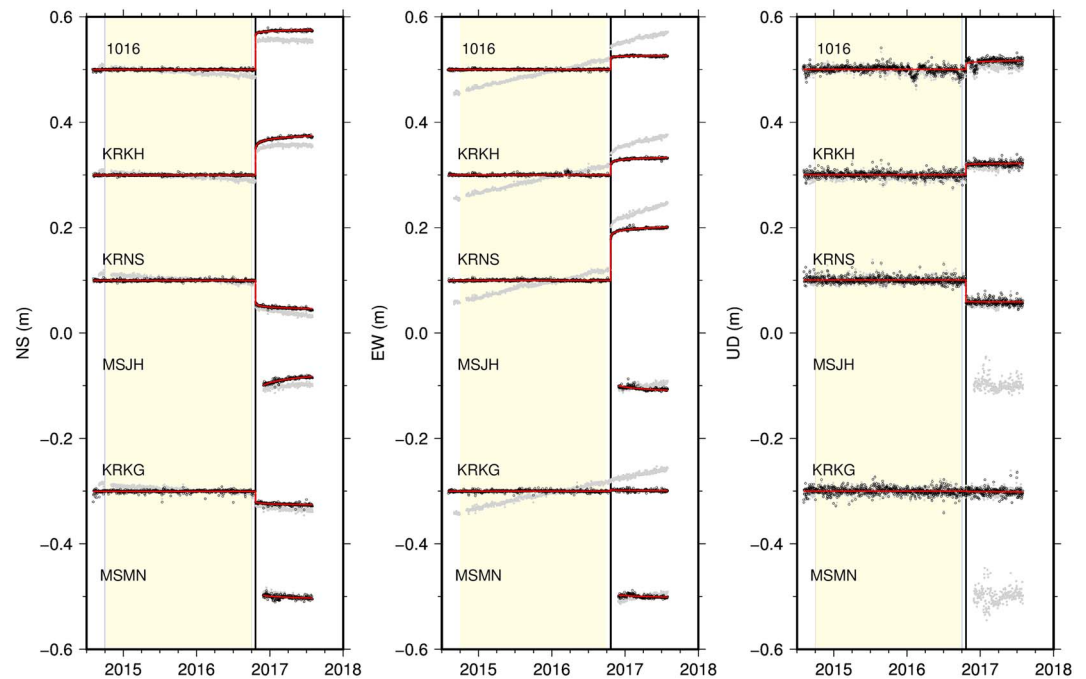
Figure 2. Coordinate time series for selected GNSS stations close to the epicenter of the 2016 Central Tottori earthquake before (gray dots) and after preseismic linear trend and annual and semiannual sinusoidal variations have been removed (black dots). Red line represents fitted function including a coseismic step and postseismic transient with a time decay constant of 2.2 days. Stations geographical location is shown in Figure 1. Vertical black lines on each plot correspond to the occurrence of the 2016 Central Tottori Earthquake.

estimated values for other inland earthquakes in Japan, such as the 2007 M_j 6.8 Chuetsu-oki earthquake (0.35 to 2.83 days; Ohta et al., 2008). We then implemented this quantity as a common value for all the stations used in this analysis and applied a linear least squares method to estimate the spatial distribution of the coseismic and postseismic displacement across the area (Figure 3 and Table 1).

Clear coseismic displacement is observed at GNSS stations around the epicentral region of the 2016 Central Tottori earthquake (Figures 3a and 3b). The largest displacement is recognized at station KRNS where horizontal displacement to the southeast of ~9 cm and subsidence of ~4 cm is observed. Large postseismic displacement pattern is observed only at stations near the epicenter of the event for 7 months (Figures 3c and 3d), which is in agreement with shallow afterslip. The largest displacement is detected very close to the epicenter at one of the stations deployed after the earthquake (MSJH; Figure 1). Maximum horizontal displacement to the northwest of 5 cm is observed, while vertical deformation is less than 1 cm in the epicentral area. The postseismic displacement is more concentrated than the coseismic one (Figures 3a and 3d), which suggests that the source for the postseismic displacement is shallower than the coseismic one. We, therefore, assume shallow afterslip as the dominant mechanism of crustal deformation in the postseismic period.

2.2. Coseismic Displacement From Accelerograms

Strong ground motions were observed during the 2016 Central Tottori earthquake by stations of the nationwide accelerometer networks, K-NET and KiK-net, operated by the NIED (Aoi et al., 2011). We use horizontal components of strong motion waveform on the ground surface at nine stations near the source region of the 2016 Central Tottori earthquake: five K-NET stations and four KiK-net stations (Figure 1).

To calculate coseismic displacement from the accelerogram data, we first use a time window of 40 s for all records and then apply a double integration in time to obtain the displacement time series (Figure 4). Velocity time series show a linear trend in time, which amplifies the displacement component. It is well known that different sources might cause systematic error on strong ground motion measurements (e.g., Iwan et al., 1985). Thus, data must be corrected for such effects.
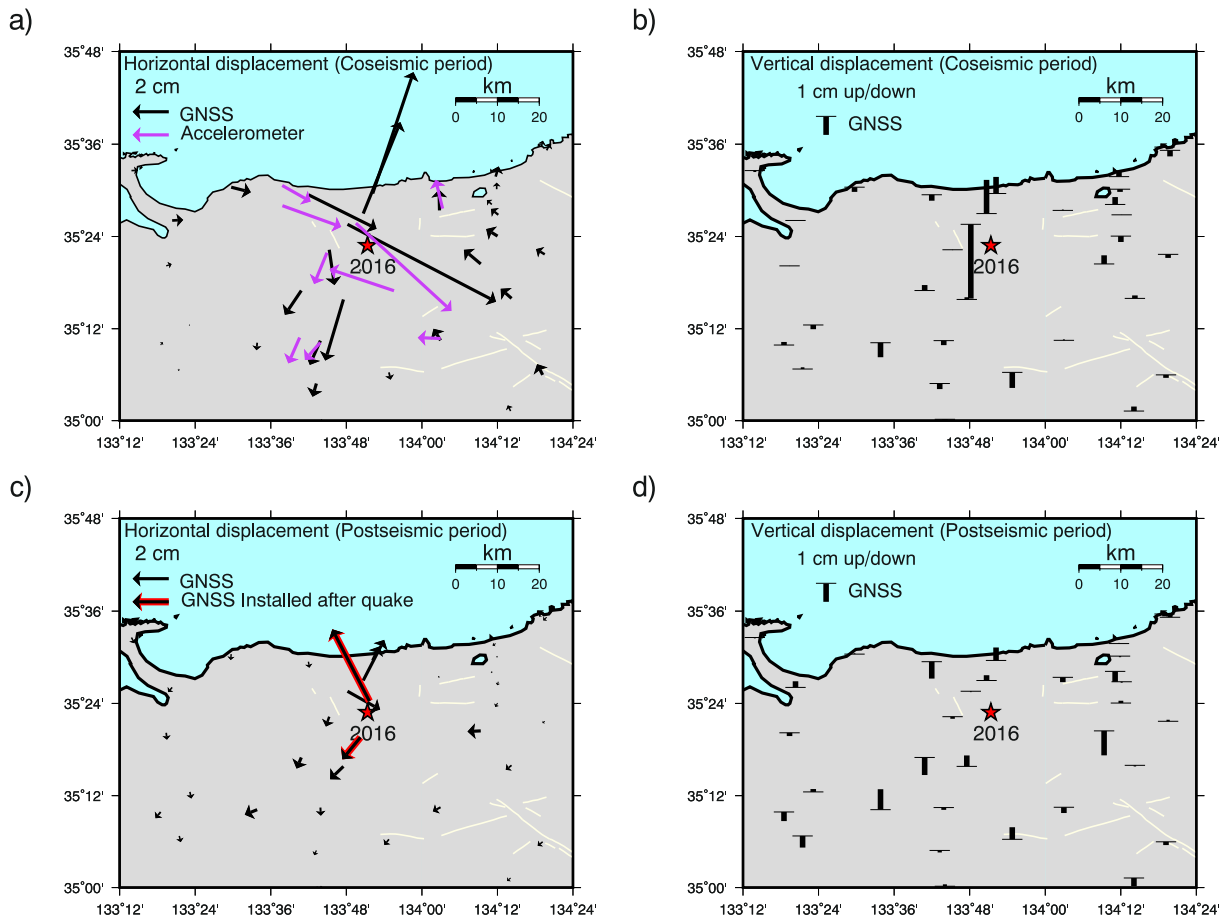
Figure 3. Observed displacement associated with the 2016 Central Tottori earthquake. Horizontal (a) and vertical (b) coseismic displacement. Black symbols denote GNSS observations, while purple arrows static displacement at K-NET and KiK-net stations. Red star denotes the hypocenter of the mainshock. Observed horizontal (c) and vertical (d) postseismic displacement for 7 months after the mainshock. Black arrows with red outlines represent GNSS stations deployed after the 2016 Central Tottori earthquake. Light yellow lines show Quaternary fault traces (Research Group for Active Faults of Japan, 1991).

Table 1

Coordinates and Observed Coseismic and Postseismic Displacements of GNSS Stations Deployed by DPRI, Kyoto University

| Station name	Longitude (°)	Latitude (°)	Coseismic displacement (cm)			Postseismic displacement (cm)		
			E-W	N-S	U-D	E-W	N-S	U-D
HNKS	133.386	35.208	-0.07 ± 0.03	-0.02 ± 0.04	-0.24 ± 0.11	0.08 ± 0.04	0.3 ± 0.05	0.16 ± 0.14
KRKG	133.755	35.371	0.29 ± 0.05	$-1.95| \pm 0.06$	-0.02 ± 0.18	-0.19 ± 0.06	-0.55 ± 0.08	-0.12 ± 0.17
KRKH	133.845	35.450	2.05 ± 0.04	5.05 ± 0.03	1.86 ± 0.14	1.16 ± 0.05	2.25 ± 0.04	0.29 ± 0.17
KRNS	133.803	35.426	8.20 ± 0.04	-4.27 ± 0.04	-4.09 ± 0.15	1.80 ± 0.05	-1.01 ± 0.05	0.05 ± 0.19
MNKK	133.721	35.081	-0.21 ± 0.03	-0.74 ± 0.03	-0.31 ± 0.12	-0.12 ± 0.04	-0.27 ± 0.04	-0.11 ± 0.15
MNYB	133.731	35.174	-0.59 ± 0.04	-1.34 ± 0.04	-0.25 ± 0.13	0.02 ± 0.05	-0.45 ± 0.05	-0.13 ± 0.16
NNHS	133.323	35.337	0.30 ± 0.03	0.10 ± 0.03	-0.01 ± 0.11	0.04 ± 0.03	-0.39 ± 0.04	-0.18 ± 0.14
NNIW	133.358	35.112	-0.06 ± 0.03	-0.09 ± 0.04	0.10 ± 0.14	0.08 ± 0.04	-0.34 ± 0.04	-0.64 ± 0.17
SMSK	133.231	35.543	0.37 ± 0.04	0.013 ± 0.03	-0.08 ± 0.11	0.17 ± 0.05	-0.32 ± 0.03	-0.05 ± 0.14
TTKH	134.200	35.401	-0.63 ± 0.03	0.39 ± 0.04	-0.32 ± 0.13	-0.13 ± 0.04	-0.22 ± 0.04	0.13 ± 0.16
TTKZ	134.202	35.447	-0.41 ± 0.03	0.33 ± 0.04	-0.01 ± 0.13	-0.07 ± 0.04	-0.19 ± 0.05	-0.05 ± 0.16
TTSK	134.198	35.503	0.00 ± 0.03	0.36 ± 0.03	-0.15 ± 0.13	0.04 ± 0.03	-0.08 ± 0.03	-0.06 ± 0.16
TTTG	134.185	35.470	-0.27 ± 0.03	0.24 ± 0.03	0.41 ± 0.14	-0.01 ± 0.04	-0.10 ± 0.04	-0.58 ± 0.17
MSJH	133.861	35.405	—	—	—	-2.05 ± 0.19	3.97 ± 0.15	—
MSMN	133.837	35.326	—	—	—	-1.22 ± 0.20	-1.00 ± 0.18	—
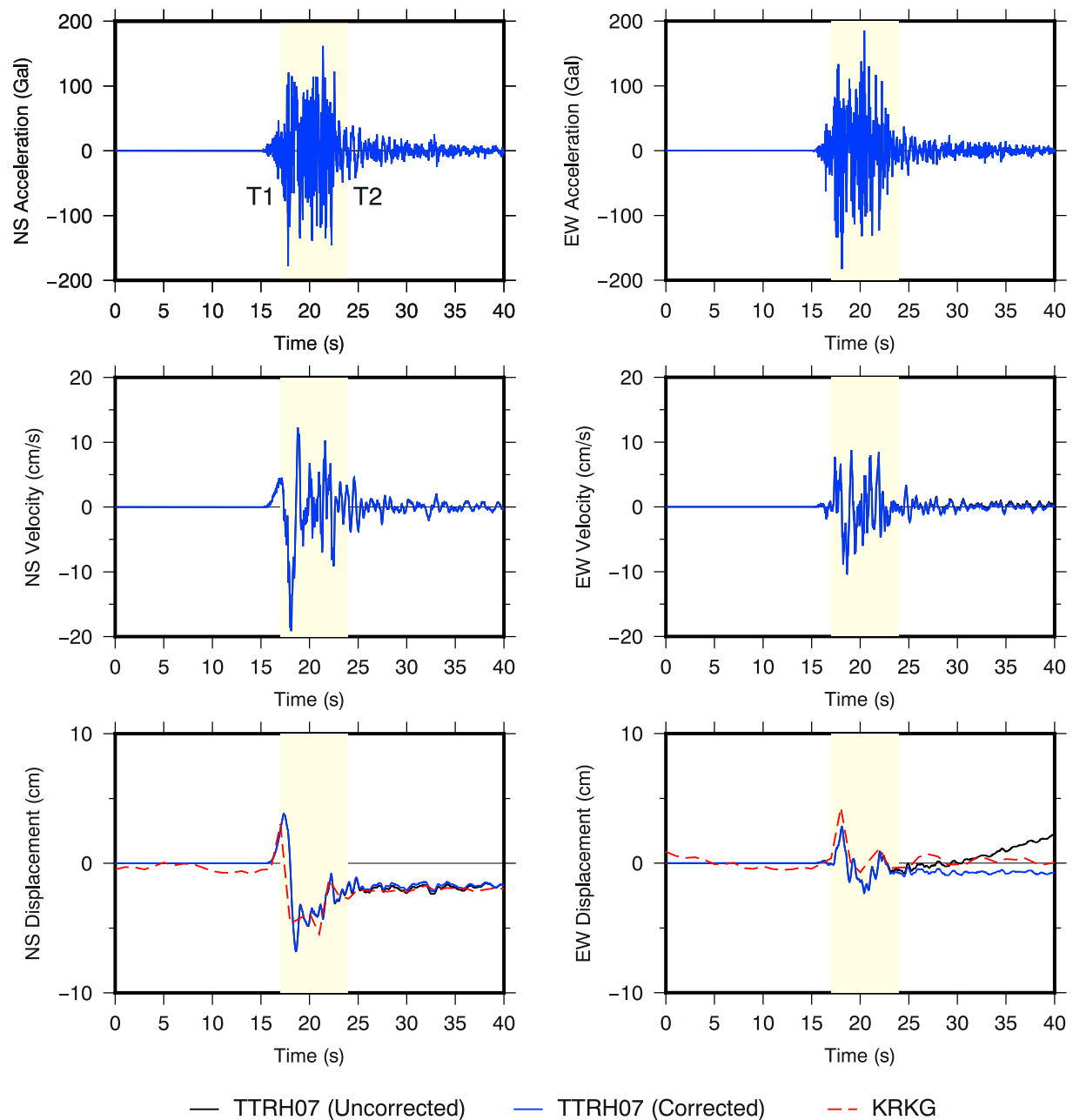
Figure 4. Recorded horizontal ground motion from the 2016 Central Tottori earthquake before (black) and after (blue) baseline corrections at KiK-net station TTRH07. Acceleration, velocity, and displacement time series are shown for the east-west and north-south components. T1 and T2 denote manual pick for the beginning and the end of the strongest shaking interval, respectively. The 1-s sampling coordinates at collocated GNSS station KRKG (red) are shown for comparison. Good correspondence between strong ground motion and GNSS data is found.

To correct the accelerograms data, we first manually pick the starting (T_1) and ending (T_2) times of the strongest shaking interval at each station (Figure 4). Then, following Iwan et al. (1985), we apply two baseline corrections to the accelerogram: one between times T_1 and T_2 (A_m) and another from T_2 to the end of the record (A_f), in our case 40 s. A_f is determined by least squares fitting of a linear function to the velocity trace (V_f) from T_2 to the end of the record ($V_f = V_o + A_f t$, where t is time), while A_m corresponds to average acceleration during the strongest shaking interval ($A_m = \frac{V_f(T2)}{(T2-T1)}$). Once corrections are applied, we double integrate the accelerograms to obtain corrected displacement time series (Figure 4). Corrections are applied so that flat

levels of displacement can be found at the end of the time series. Finally, a step function is fit to the corrected displacement to determine the coseismic static displacement.

For quality control, we evaluate the correspondence between collocated GNSS and accelerometer stations. The corrected displacement from an accelerometer station is in agreement with 1-s sampling displacement at a nearby GNSS station (Figure 4). The spatial pattern of the permanent displacement from accelerogram data seems to be in agreement with GNSS displacement as well (Figure 3a). Clear coseismic displacement is observed at the stations near the epicenter of the 2016 Central Tottori earthquake. The largest displacement is recognized at station TTR005 (Figure 1), where horizontal motion of 5 cm to the southeast is observed.

2.3. InSAR

We use L-band Synthetic Aperture Radar (SAR) images acquired by the Advanced Land Observing Satellite-2, operated by the Japan Aerospace Exploration Agency (JAXA), to monitor the spatial distribution of the coseismic deformation of the 2016 Central Tottori earthquake. Three pairs of SAR images are processed in order to generate coseismic interferograms. The interferograms after phase unwrapping map the line of sight displacement between the ground and the satellite around the source region of the mainshock in Tottori Prefecture (Figure 5a). Images from both descending and ascending orbits are used, whose acquisition parameters are given in Table 2. SAR data indicate coseismic displacement concentrated within 20 km from the epicentral area. It is interesting that coseismic line of sight displacements are observed on either east or west side of the epicenter depending on incident angle and look direction. The largest displacement in the descending interferogram is about 8 cm, to the east of the epicenter of the 2016 Central Tottori earthquake, while approximately 7 cm of slip is observed to the west from the ascending orbit. No major discontinuities are detected across the area, which is concordant with no reported surface ruptures. A significant deformation limited to the vicinity of the source indicates that coseismic slip occurred at shallow depths (Figure 5a). We examine several interferograms for a postseismic period but found no significant deformation.

3. Deformation Modeling

We estimate the coseismic and postseismic slip distribution of the 2016 Central Tottori earthquake by performing a linear inversion of available data sets. Coseismic slip distribution inversions includes the previously described InSAR, and GNSS displacement data, while postseismic distribution is only assessed using GNSS data, due to the limited resolution of the InSAR data in the postseismic period. Static displacement data at accelerometer stations are only use for comparison purposes.

As a priori information geometry of the fault and constraint of the smoothness of the slip distribution is given to minimize the data misfit. A priori fault model is estimated by assuming a uniform slip in a homogeneous half-space (Okada, 1985) and preforming a nonlinear inversion of the GNSS data to optimize initially assigned values for all the fault parameters (Matsu'ura & Hasegawa, 1987; Table 3). Once optimal geometry of the fault is determined, we perform a linear inversion of available data to estimate slip distributions in the coseismic and the postseismic period of the 2016 Central Tottori earthquake following Nishimura (2009).

For the linear inversion, we extend the a priori fault model along the strike and along the dip directions in order to assess the extent of the coseismic and postseismic slip. The fault area is divided into 12×12 rectangular subfaults of 1-km $\times$ 1-km dimensions. The slip angle is not fixed for the inversion. Model displacement is calculated by assuming a homogeneous elastic half-space (Okada, 1985). The smoothness of the slip distribution is given by

$$\sum_l \sum_m \sum_n \left(\left(2s_{l,m,n} - s_{l,m-1,n} - s_{l,m+1,n} \right) + \left(2s_{l,m,n} - s_{l,m,n-1} - s_{l,m,n+1} \right) \right)^2, \tag{2}$$

where $s_{l,m,n}$ is the slip amount on the mth and nth subfaults along the strike and dip direction (Nishimura, 2009). $l = 1$ and 2 represents dip and strike component, respectively. Edge constraints were not applied for the coseismic inversion. In the postseismic model, the fault was allowed to slip on the surface but not on the other edges. Additionally, a hyperparameter to control the weight of the smoothness constraint is determined as the value that minimizes the Akaike's Bayesian Information Criterion (Akaike, 1980).
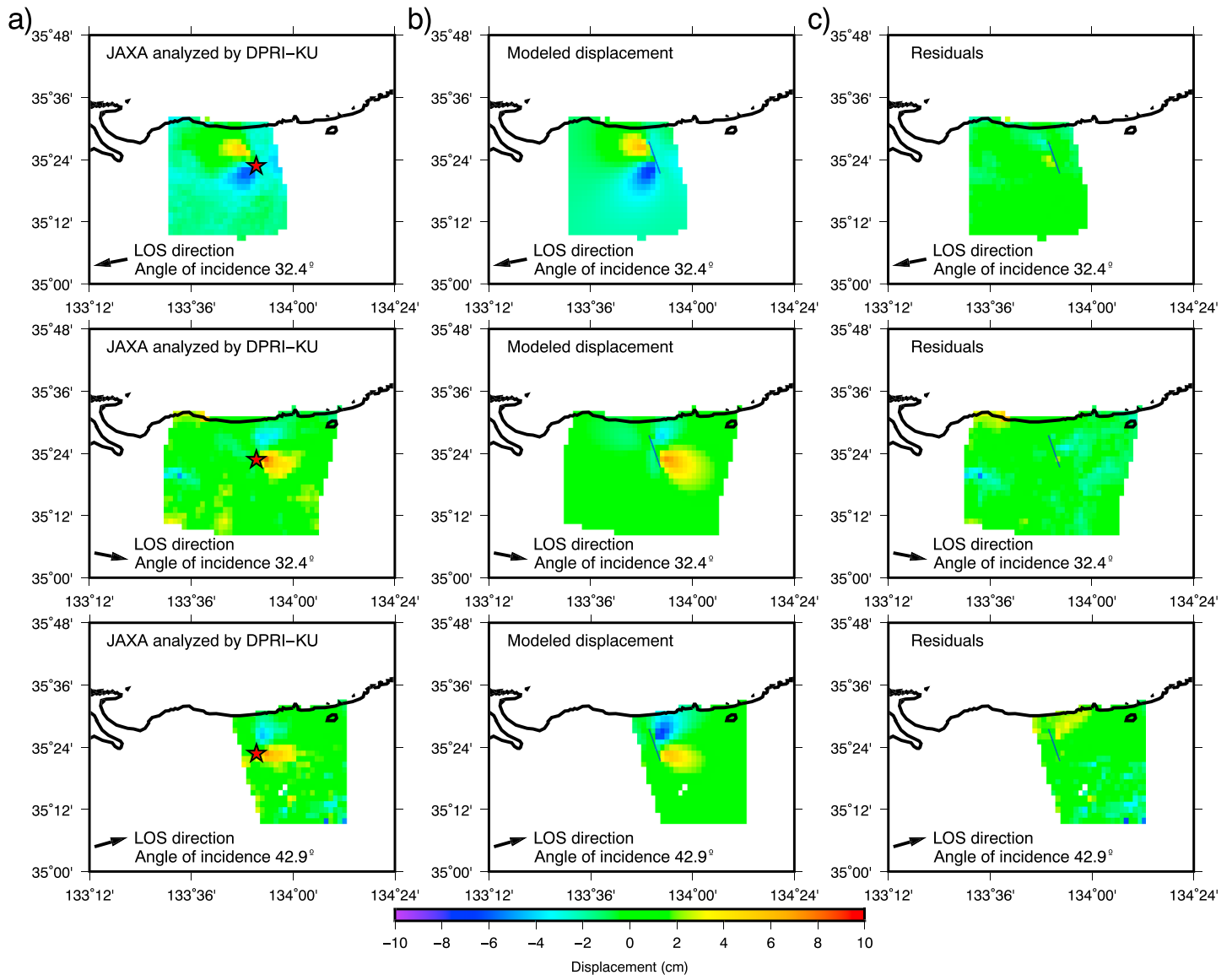
Figure 5. (a) InSAR images for ascending and descending orbits covering the source region of the 2016 Central Tottori earthquake. Red star denotes the hypocenter of the mainshock. (b) Modeled displacement associated with coseismic slip distribution estimated in this study. (c) Residuals between the observed and the estimated displacement. JAXA = Japan Aerospace Exploration Agency; LOS = line of sight.

Since different types of observations are employed for the coseismic slip distribution, weighting of the data must be studied. Uncertainty of GNSS data corresponds to the diagonal values of the covariance matrix during the linear regression fitting, when assuming uncorrelated errors. InSAR data for the inversion are

Table 2
Parameters of Observation of ALOS-2/PALSAR-2 Used in This Study

Satellite orbit flight direction/look direction	Master image	Slave image	Incident angle (°)	Azimuth (°)	Perpendicular baseline (m)
P122-F730-740 Ascending, left	2015/11/7	2016/10/22	42.9	N74E	172.6
P128-F700 Ascending, right	2016/5/23	2016/10/24	32.4	N259E	54.3
P22-F2900, Descending, right	2016/8/3	2016/10/26	32.4	N101E	1.4

Note. Dates are formatted as YYYY/MM/DD.

Table 3
Parameters of Fault Models Estimated and Used in This Study

Event	Latitude (°)	Longitude (°)	D (km)	W (km)	L (km)	Strike (°)	Dip (°)	Rake (°)	Slip (m)	Reference
2016	35.445	133.837	1.6	10.2	8.9	160.4	88.0	−2.0	0.75	Nonlinear inversion
2000	35.357	133.305	0.9	20.5	9.8	152.0	86.0	−7.0	1.4	Sagiya et al. (2002)
1983	35.430	133.910	5.0	6.0	5.0	140.0	85.0	0.0	0.5	Oike (1987)
1943	35.440	134.000	0.0	13.0	33.0	80.0	90.0	180.0	2.5	Kanamori (1972)

Note. "D," "W," and "L" denote upper edge depth, width, and length of rectangular faults, respectively.

downsampled with the Quadtree algorithm, and total data points for InSAR are 1942. Uncertainty of Advanced Land Observing Satellite data are usually within a few centimeters. We perform multiple geodetic inversion by considering different values of uncertainty of InSAR data ranging between 1 and 4 cm. Large uncertainty values result in significant systematic residuals near the source region of the 2016 Central Tottori earthquake (~6 cm; Figure S1 in the supporting information), while smaller values result in reducing them. Thus, we continue our analysis of the InSAR data with a nominal uncertainty of 2 cm (Figure 5).

Once the coseismic and postseismic slip distribution are determined, we perform a checkerboard test to assess the ability of the used geodetic data to resolve slip at depths. To do this, we perform a forward modeling of the surface displacement due to assigned checkerboard slip configuration and add Gaussian errors to the observations to simulate observation errors. We assume synthetic errors as those of the observation used for each inversion. The slip values for the checkerboard test are assigned as those of the maximum slip in the coseismic and postseismic distribution, respectively. Then, the synthetic displacement is inverted using the same method as for the observations, and a qualitative comparison of the input and output slip distribution is discussed.

4. Results and Discussion

4.1. Coseismic Fault Model

Modeled displacement and coseismic slip distribution of the 2016 Central Tottori earthquake is shown in Figures 5b and 6a–6c. Major slip area is constrained within a depth of 4 to 10 km. A large slip region with a maximum estimated slip of 1.28 m extends to the northwest of the rupture source from the hypocenter, without reaching the surface. Estimated slip errors range from 5 to 35 cm and are smaller in the shallow region (Figure S2). The total seismic moment in the model region is 2.15×10^{18} N·m (M_w 6.15), assuming a rigidity of 30 GPa. This seismic moment release is in agreement with the moment magnitude provided by moment tensor analysis of F-net solutions (M_w 6.2; National Research Institute for Earth Science and Disaster Resilience, 2016).

The checkerboard resolution test shows that the coseismic slip distribution on the fault plane is well resolved for a slip area of 6 km × 6 km and greater (Figures S3, S4, and S5). At shallow depths, the data inversion can resolve slip areas as small as 3 km × 3 km. However, resolution at depths is limited.

Comparison of the model and observed displacements used for this inversion shows that the general characteristics of the deformation pattern are reproduced by the current model (Figures 5, 6a, and 6b). Residuals of InSAR data are within the uncertainty values as well (Figure 5c). Predicted displacement direction for accelerometer stations is in agreement with observations, although differences up to 2 cm are recognized at some stations (Figure 6a).

As mentioned before, two coseismic slip models of the 2016 Central Tottori earthquake utilizing strong ground motion data have been reported. However, the estimated distributions are not consistent with each other. Kubo et al. (2017) reported a complex source region with two main slip patches below 4-km depth, while Ross et al. (2018) proposed a deeper rupture concentrated in a narrow region. Ross et al. (2018) suggested that the results from Kubo et al. (2017) had less spatial resolution due to the lack of stations in the forward direction for their inversion. The inclusion of such stations puts a constraint on the directivity of the main slip path (Ross et al., 2018). Our model, based on the inversion of near-field static coseismic displacement data, does not favor the results from either seismic inversion. It has been shown that slip in our
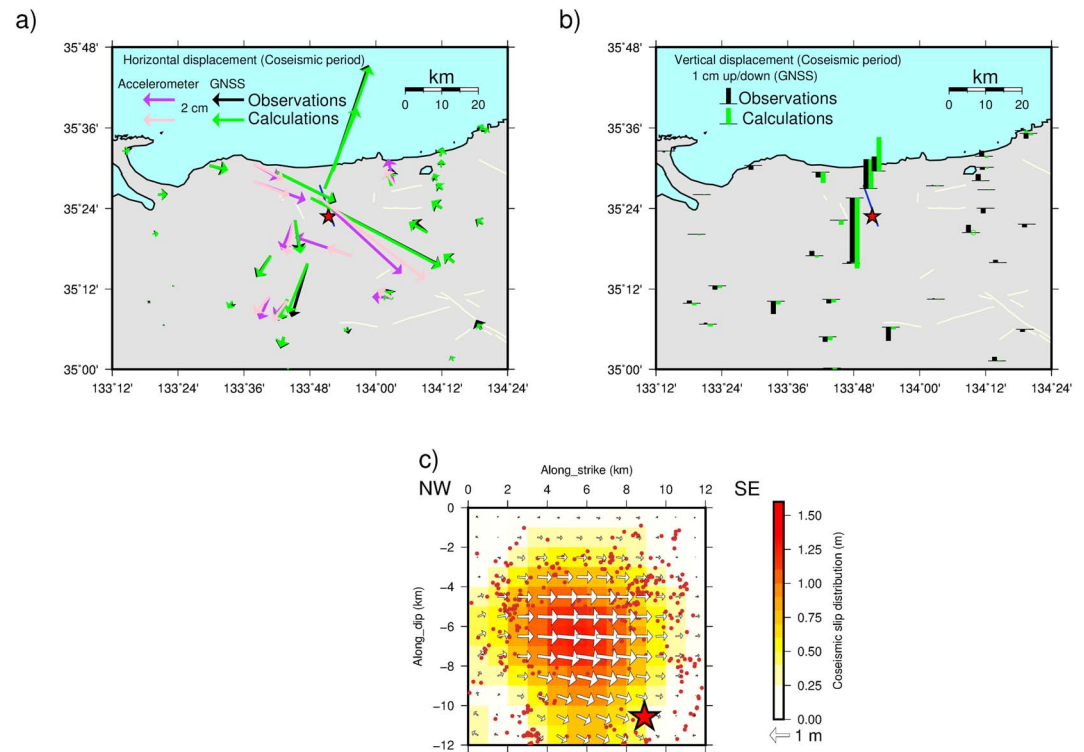
Figure 6. Observed and estimated horizontal (a) and vertical (b) coseismic displacement associated with the 2016 Central Tottori earthquake. Black symbols denote GNSS observations, while purple arrows static displacement from accelerograms at K-NET and KiK-net stations. Predicted displacement is indicated by green symbols for the GNSS data and pink arrows for K-NET and KiK-net stations. Blue line indicates surface projection of the estimated fault model. Thin yellow lines show Quaternary fault traces (Research Group for Active Faults of Japan, 1991). (c) Estimated coseismic slip distribution. Brown dots indicate aftershocks within 2 km from the fault, 1 month after the earthquake (Iio et al., 2018). Red star denotes the hypocenter of the mainshock in all the plots.

model occurs at shallow depths to the northwest of the mainshock, and our resolution tests indicate limited resolution at depth for patches smaller than 6 km × 6 km. To evaluate the possibility of deep and narrow slip, we perform the following tests: we first simulated the source models of Kubo et al. (2017) and Ross et al. (2018) and estimated the expected displacement at the GNSS sites from such distributions (Figures S6 and S7). We found that neither model can reproduce near-field deformation at the GNSS sites. To test the model described by Ross et al. (2018), we perform an inversion of our data set confining slip within a depth of 7 to 14 km. We also extend the fault plane to the southeast. Such test indicates that the total seismic moment (3.28×10^{19} N·m, M_w 6.94) is unrealistically large, and although it is possible to roughly reproduce the observed displacements by a deep heterogeneous slip distribution, large residuals are observed near the source region (Figures S8 and S9).

It is clear that deep sources of deformation cannot explain the geodetic data; however, since our data set cannot resolve patches with a width smaller than 6 km, the width of the large slip area can be another cause of controversy. To evaluate this parameter, we perform geodetic inversions considering a length for the assumed fault area reducing to 8 km and 4 km at the centroid of the current geodetic solutions (Figures S10 to S13). These tests showed that near- and far-field geodetic observation can be well explained by an 8-km-long fault (Figures S10 and S11), while a narrow 4-km-long source causes larger residuals near the source region (Figures S12 and S13). Thus, a confined source as described by Ross et al. (2018) is not favored. Aftershock distributions associated with each model will be discuss later.

It is true that the resolving power of seismic data at depths is greater than that of geodetic data. However, it is also true that the spatiotemporal parametrization of the rupture employed during the seismic inversion results in a large number of free parameters which can add bias to the solution. Also, rupture models depend strongly on the hypocenter location. Therefore, if hypocenter data are not correct, subsequently, slip

distributions can have bias. Comparison of our model with the aftershock distribution 1 month after the event, relocated by Iio et al. (2018), shows little overlapping of the largest main shock slip and active seismicity surrounding the large slip area (Figure 6c). Iio et al. (2018) used data from dense temporal seismic stations and reported that relocated aftershocks become shallower by 2 km than those estimated only with permanent stations (e.g., Kubo et al., 2017). We also notice that the distributions of coseismic slip and aftershocks on Ross et al. (2018) seem to be shifted deeper than those of Iio et al. (2018). Absolute location of slip distribution using Empirical Green's function method depends on the location of initial rupture (e.g., mainshock hypocenter), which might be the cause of inconsistencies between our model and Ross et al's.

Geodetic data used in this study improve the spatial coverage of the near-field region. In contrast with seismic waveforms, permanent displacement is rather insensitive to subsurface elastic structures (e.g., Lindsey & Fialko, 2013). Therefore, coseismic near-field displacement observed from geodetic tools is robust evidence for the shallow source as examined above. We cannot constraint the displacement at depths, but shallow displacement is fundamental to explain deformation due to the 2016 Central Tottori earthquake. Apparent depth inconsistency between our model and that of Kubo et al. (2017) can be related with lack of spatial resolution of the seismic network.

4.2. Postseismic Model

Modeled displacement and postseismic slip distribution of the 2016 Central Tottori earthquake is shown in Figures 7a–7c. Estimated deformation patterns are in agreement with the observation. The observed displacement is concentrated in the epicentral region (Figures 7a and 7b). Afterslip distribution indicates distributed afterslip in the shallow portion of the source fault, above the area of large coseismic slip, which is even shallower than aftershocks (Iio et al., 2018; Figure 7c). Maximum afterslip of 14 cm was observed near to the surface, with virtually no slip at depths greater than 7 km. Estimated slip errors are between 3 and 15 mm (Figure S14). This limited distribution of afterslip supports the idea of an immature intraplate environment reported by Ross et al. (2018). The source fault of the 2016 earthquake is so immature that afterslip is restricted from propagating widely, which is in contrast to widespread afterslip on mature subduction faults (e.g., Miyazaki et al., 2004).

The total seismic moment release in the postseismic period is 2.34×10^{17} N·m (M_w 5.51). This means that ~11% of the seismic moment released by the mainshock is released in the form of afterslip. Complementary spatial pattern between the coseismic and postseismic slip implies afterslip driven by coseismic stress change.

The checkerboard resolution test for the afterslip distribution is similar to those for the coseismic distribution. Afterslip distribution on the fault plane is only fairly resolved at shallow depths for a slip area of 6 km × 6 km and greater (Figure S15). Resolution at depths is limited. However, shallow displacement is necessary to explain the geodetic observations.

Near-field observations are fundamental in order to study postseismic deformation of intermediate inland earthquakes, such as the 2016 central Tottori earthquake. DPRI sites close to the source fault are essential to estimate detailed afterslip distribution. Two DPRI sites installed after the earthquake also give an additional constraint of afterslip distribution despite these stations that cannot provide direct information on the early stages of the postseismic slip. To evaluate the contribution of the DPRI stations into the postseismic model, we estimated afterslip distributions considering only GNSS stations from the nationwide GNSS network (GEONET) and evaluated the estimated displacement at sites closer to the fault (Figure S16). Slip distributions with and without DPRI sites indicate distributed afterslip in the shallow portion of the source fault; however, differences are observed within the first 2 km of depth in the fault. Slip distribution using a dense GNSS network indicates concentrated slip within 1 km at surface (~14 cm; Figure 7), which was not recovered using GEONET (Figure S16). Such constrains can only be obtained with a spatially dense GNSS network, as evidenced by the fact that near-fault displacement at stations installed after the earthquake could not be retrieved when using GEONET data alone. Estimated slip errors also increase significantly when dense GNSS data are not considered (Figure S16). DPRI sites installed after the earthquake are close to the largest afterslip patches and show a direct evidence of shallow afterslip. Thus, a dense GNSS network allocates additional constraints to the spatial distribution of the afterslip.
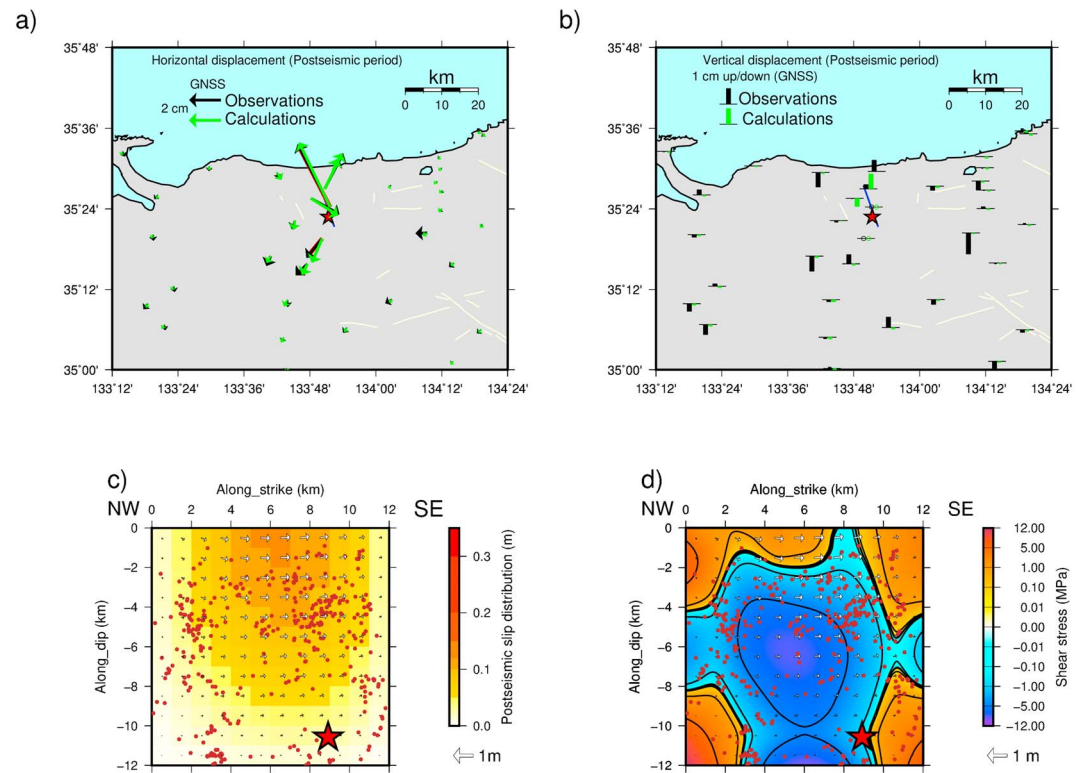
Figure 7. Observed and estimated horizontal (a) and vertical (b) postseismic displacement 7 months after the 2016 Central Tottori earthquake. Black symbols indicate observation, while green symbols estimated displacement. Observed displacement at stations deployed after the earthquakes is denoted with red outline. Blue line indicates surface projection of the estimated fault model. Thin yellow lines show Quaternary fault traces (Research Group for Active Faults of Japan, 1991). (c) Estimated slip distribution in the postseismic period. (d) Shear stress change on the fault plane caused by the mainshock. Brown dots indicate aftershocks within 2 km from the fault, 1 month after the earthquake (Iio et al., 2018). Red star denotes hypocenter of the mainshock in all the plots.

4.3. Aftershock Distribution

A large earthquake causes stress change in its surroundings. Such coseismic stress change may be too small to cause another earthquake. However, in case another fault has been already loaded enough, the stress change may trigger additional earthquakes.

One vastly used criteria to evaluate stress triggering correspond to the Coulomb stress change caused by an earthquake (ΔCFF; e.g., King et al., 1994)

$$\Delta\sigma_{\mathrm{CFF}} = \Delta\tau - \mu^{'}\Delta\sigma_n \tag{3}$$

where $\Delta\tau$ is the shear stress change on the fault plane, $\Delta\sigma_n$ the normal stress change (compression is positive), and $\mu^{'}$ the effective friction coefficient on the fault plane.

We estimate ΔCFF due to the 2016 Central Tottori earthquake over the two possible earthquake nodal planes of the best double-couple solution determined from F-net focal mechanisms (National Research Institute for Earth Science and Disaster Resilience, 2016). Stress change is calculated in an elastic half-space (Okada, 1992). We consider optimized models with areas of 12 km × 12 km, 8 km × 12 km, and 4 km × 12 km, which are examined in section 4.1 as the source models. ΔCFF calculations at a depth of 5 km utilizing the estimated slip distribution in this study as the source model indicate good correspondence between the horizontal location of the aftershocks and the areas of positive stress change in the far field (Figure 8). Aftershocks are aligned with the mainshock fault. In the near field, differences on the stress change distribution can be observed near the source region according to the width constraint on the slip distribution. Aftershocks on a conjugated fault occur at the southeast end of the mainshock fault, and it is not possible to explain such seismicity by all the models. Negative stress change at the south end of the mainshock
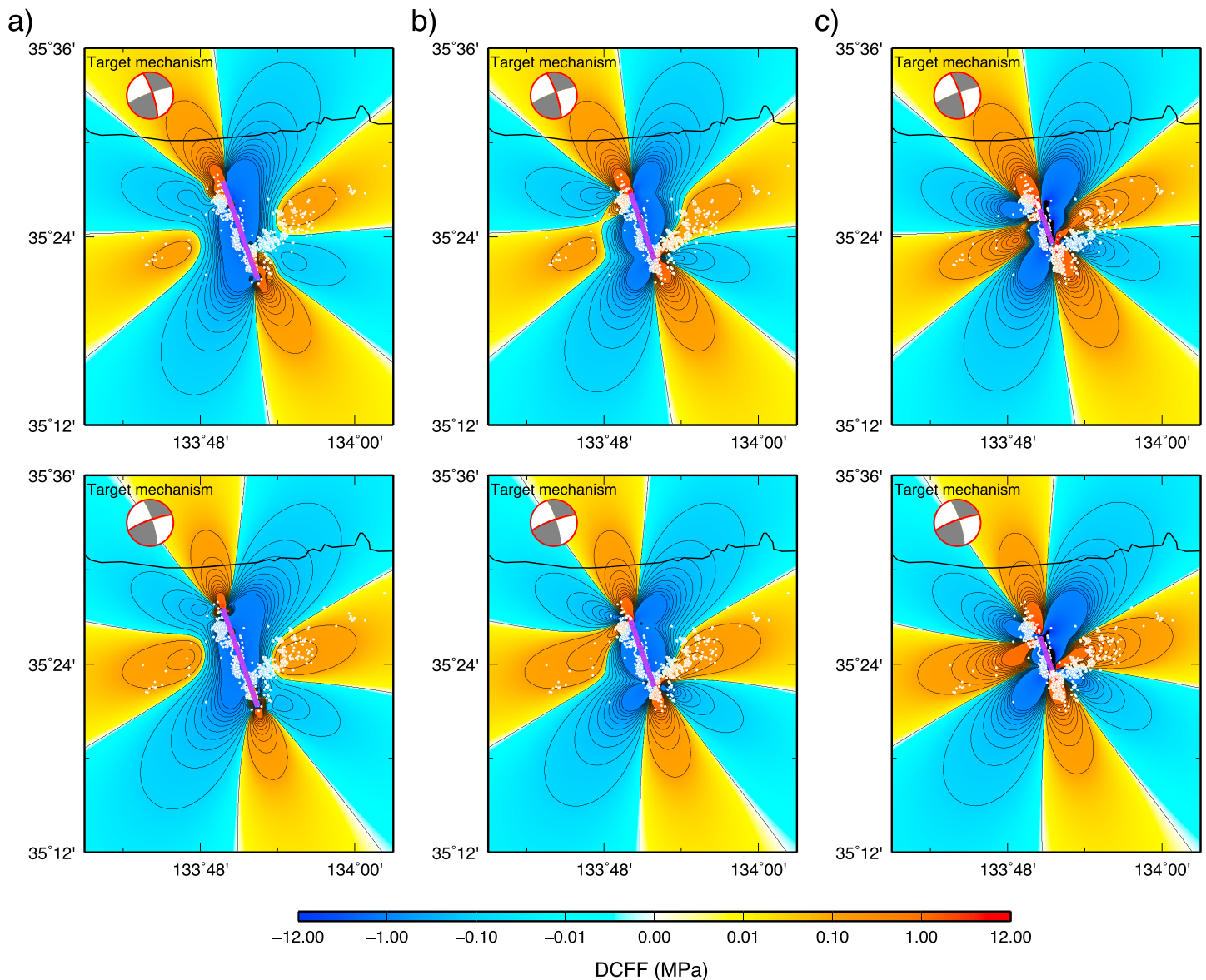
Figure 8. Near-field Coulomb stress change at 5-km depth induced by the 2016 Central Tottori earthquake on faults having the configuration shown by the focal mechanism on each sub-figure. (a) 12-km × 12-km source, (b) 8-km × 12-km source, (c) 4-km ×°12-km source. Contour lines every 0.1 MPa between −1 and 1 MPa are drawn. Efficient friction coefficient of 0.4 and a rigidity of 30 GPa are assumed. Purple line indicates surface of the estimated fault model. Aftershock distribution 1 month after the earthquake is shown by white circles (Iio et al., 2018). Aftershock distribution is reasonably explained by estimated coseismic model.

fault is observed when the source fault is 12 km × 12 km (Figure 8a), failing to explain near-field off-fault seismicity. A slip distribution with an area of 8 km × 12 km, similar to the major slip area in our model, indicates positive stress change where aftershock activity was observed, including seismicity in a conjugated fault at the south of end of the mainshock (Figure 8b), showing that the aftershock distribution is in agreement with stress change caused in the region by the mainshock. A short fault patch fails to explain near-field aftershocks on a conjugated fault (Figure 8c).

Relocated aftershock distributions in November 2016 (Iio et al., 2018) are overlapped on the coseismic and postseismic slip distributions, as well as on the shear stress change plot (Figures 6c, 7c, and 7d). During the months following the mainshock, aftershocks occurred mostly to the north of the mainshock hypocenter and are concentrated at depths greater than 1.5 to 12 km. The number of aftershocks within the area of large coseismic slip is small in comparison with the total number of aftershocks. Most aftershocks occurred in the region surrounding the area of large coseismic slips. Reduced aftershock activity in the area of the largest
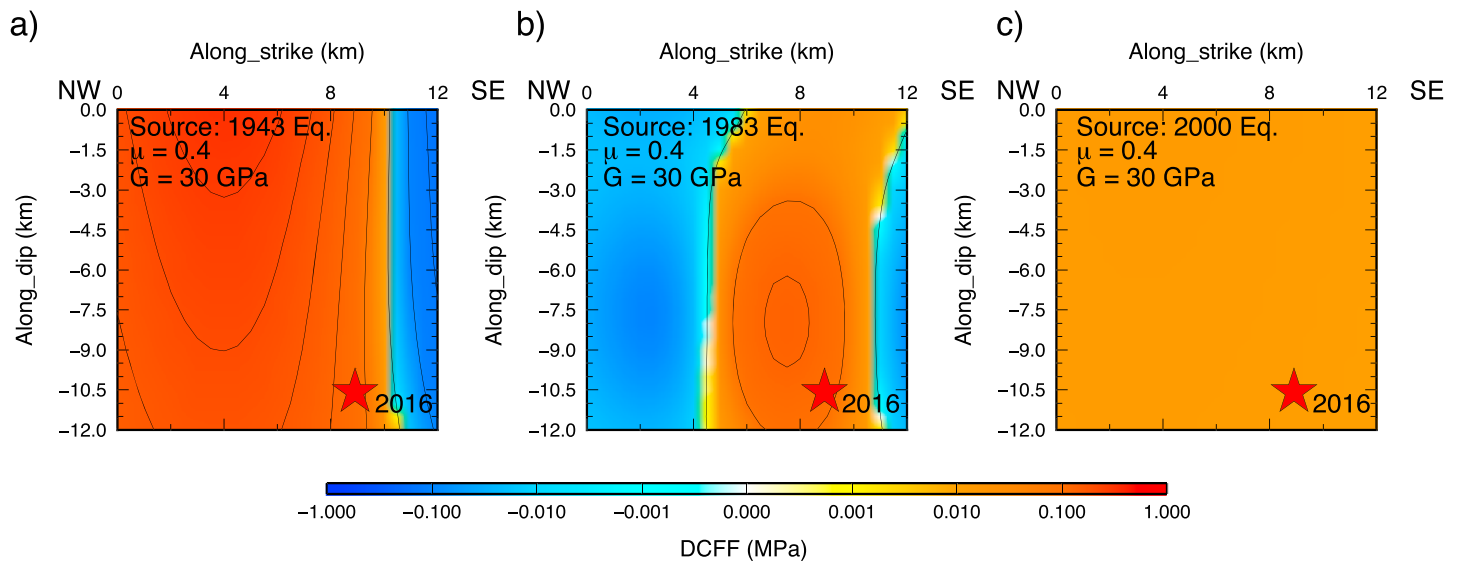
Figure 9. (a–c) Coulomb failure function change over the 2016 Central Tottori earthquake fault plane in response to the 1943 Tottori earthquake (*Mj* 7.2), the 1983 Central Tottori earthquake (*Mj* 6.2), and the 2000 Western Tottori earthquake (*Mj* 7.3). Contour lines every 0.1 MPa between −1 and 1 MPa are drawn. Red star denotes the hypocenter of the mainshock of the 2016 Central Tottori earthquake. Efficient friction coefficient (μ) of 0.4 and a rigidity (G) of 30 GPa are assumed.

coseismic slip has been previously reported for crustal earthquakes (e.g., Ohmi et al., 2002). Low aftershock activity in coseismic slip areas suggests that large amount of stress is released during the mainshock rupture, inhibiting this area from slipping anymore. On the other hand, areas with small coseismic slip appear to have aftershock concentration, indicating stress loading in the area caused by the mainshock. Postseismic slip distribution does not have concentrated slip in the area of large aftershocks. This could be associated with the limited resolution of the GNSS sites at depths.

4.4. Shear Stress Change on the Fault Plane Due to the Mainshock

To investigate the relationship between the mainshock of the 2016 Central Tottori earthquake and the estimated afterslip distribution, we calculate the shear stress change on the source fault. The estimated coseismic slip distribution in this study was used to calculate the shear stress change under the assumption of homogeneous elastic half-space (Okada, 1985; Figure 7d). Shear stress range from −9.0 MPa, around the area of the largest coseismic slip, to 4.6 MPa in the surrounding region (Figure 7d). Increase of shear stress change is predicted immediately around the area of large stress drop. Aftershock activity is low in the area of the largest stress drop, and afterslip as well as aftershocks occurred in an area where the coseismic stress increase is predicted, implying postseismic slip and aftershocks driven by coseismic stress change (Figure 7d). However, they occurred not only in the area of stress increase but also in that of stress decrease. It may be attributed to a limited resolving power of the estimated coseismic and postseismic slip.

4.5. Preseismic Coulomb Stress Change on the Source Fault

Several earthquakes have affected crustal deformation in the Tottori prefecture in the past century. Most important events include the 1943 Tottori earthquake (M_j 7.2), the 1983 Central Tottori earthquake (M_j 6.6), and the 2000 Western Tottori earthquake (M_j 7.3; Figure 1). Due to the conjugate Riedel shear configuration present in the SSZ (Nishimura & Takada, 2017), it is important to evaluate whether or not the recent events in the area played an important role in the occurrence of the 2016 Central Tottori earthquake taking the interconnection between fault systems in the region into account.

We use ΔCFF as an indicator to examine the interaction between recent earthquakes and the 2016 Central Tottori earthquake. Coseismic fault models of the 1943, 1983, and 2000 events are taken from previous studies (Table 3). We assumed a μ' of 0.4 (King et al., 1994) and evaluated the ΔCFF on the coseismic fault of the 2016 Central Tottori earthquake. We, then, compared these results with the tectonic stress loading rate in the SSZ to assess the significance of the triggering effect over the 2016 event.

The calculated ΔCFF over the 2016 fault is shown in Figure 9. ΔCFF caused by the 1943 Tottori earthquake is positive on the majority of the fault plane of the 2016 Central Tottori earthquake except for the SE end of the fault plane, where negative static stress change is predicted (Figure 9a). Stress change ranges from −0.41 to 0.55 MPa on the fault plane. Stress change at the hypocenter location is 0.15 MPa. ΔCFF caused by the 1983 Tottori earthquake on the rupture plane of the 2016 Central Tottori earthquake indicates positive change on the central part of the fault plane, where the hypocenter of the 2016 event is located, while negative ΔCFF is observed on the edges of the fault plane (Figure 9b). Stress change ranges from −0.12 to 0.21 MPa on the fault plane. Stress change at the hypocenter location is 0.15 MPa. ΔCFF caused by the 2000 Western Tottori earthquake over the 2016 event is positive over the whole fault plane (Figure 9c). However, the stress change is rather small, ranging from 0.01 to 0.02 MPa, due to the large distance separating the events (Figure 1). Stress change at the hypocenter location due to the 2000 Western Tottori earthquake is 0.02 MPa. The fact that all the events caused positive ΔCFF at the hypocenter depth of the 2016 Central Tottori earthquake indicates that these events accelerated the occurrence of the 2016 earthquake, showing the great mechanical interaction of the fault systems in the SSZ.

In order to assess quantitatively the advance in time of the 2016 Central Tottori earthquake with respect to its predecessor events, we proceeded to divide the total ΔCFF (i.e., 0.38 MPa) of three earthquakes at the hypocenter location by the average tectonic loading in the SSZ, where the 2016 event occurred. Analysis of preseismic velocities in the SSZ indicates a shear accumulation rate of approximately 5 mm/year over a width of 30 km (e.g., Nishimura & Takada, 2017). Assuming a rigidity of 30 GPa in the area, the shear stress accumulation rate is 5 kPa/year. This rate roughly agrees with coseismic stress drop (~9 MPa; Figure 7d) divided by a recurrence interval (~300 years) from two M6.5–6.8 earthquakes in central Tottori in 1710 and 1711 (Usami, 1996). When the cumulative ΔCFF at the hypocenter location is divided by the shear stress accumulation rate in the SSZ, it appears that the occurrence of the 1943, 1983, and 2000 earthquakes advanced by approximately 66 years of the 2016 Central Tottori earthquake.

5. Conclusion

We analyze available GNSS, InSAR, and static displacement data from accelerometers in the San-in region of southwestern Japan, to estimate coseismic and postseismic slip distributions of the 2016 Central Tottori earthquake. Our findings can be summarized as follows.

1. Coseismic slip distribution of the 2016 Central Tottori earthquake indicates one patch of large slip to the northwest of the hypocenter location. Our model is not consistent with previous models obtained from seismic data inversion (Kubo et al., 2017; Ross et al., 2018). Although our resolution is poor at depth, synthetic tests showed that shallow slip is necessary to explain the geodetic observation. Lack of resolution might result in smoother pattern distributed over a larger area; however, stress transfer of an 8-km × 12-km fault model can explain off-fault seismicity. Also, most aftershocks relocated by Iio et al. (2018) occur outside the area of the largest coseismic slip in our model, in agreement with stress change caused by the earthquake.
2. Postseismic deformation decays quickly after the earthquake. Shallow afterslip is responsible for the postseismic deformation of the 2016 Central Tottori earthquake. Stress change caused by the mainshock seems to be the main mechanism driving the postseismic slip. Large afterslip is constrained near surface within 2 km. Restricted slip propagation in the postseismic period suggests that the source fault of the 2016 Tottori earthquake is immature. DPRI stations provided additional information to constrain the spatial distribution of the slip pattern. Densification of GNSS network is important to study postseismic deformation of inland events.

References

Akaike, H. (1980). Likelihood and the Bayes procedure. In J. M. Bernardo, M. H. DeGroot, D. V. Lindley, & A. F. M. Smith (Eds.), *Bayesian statistics* (pp. 143–166). Valencia, Spain: University Press.

Aoi, S., Kunugi, T., Nakamura, H., & Fujiwara, H. (2011). Deployment of new strong motion seismographs of K-NET and KiK-net. In S. Akkar, P. Gülkan, & T. van Eck (Eds.), *Earthquake data in engineering seismology. Geotechnical, geological, and earthquake engineering* (Vol. 14, pp. 167–186). Dordrecht, Netherlands: Springer. https://doi.org/10.1007/978-94-007-0152-6_12

Bertiger, W., Desai, S., Haines, B., Harvey, N., Moore, A. W., Owen, S., & Weiss, J. P. (2010). Single receiver phase ambiguity resolution with GPS data. *Journal of Geodesy*, *84*, 327–337. https://doi.org/10.1007/s00190-010-0371-9

Iio, Y., Matsumoto, S., Iidaka, T., Kurashimo, E., Sakai, S., Yamashita, Y. (2018). *Aftershock observation group of the 2016 Central Tottori Earthquake, aftershock observation of the 2016 Central Tottori Earthquake.* Paper presented at the 2018 Japan Geoscience Union Meeting, Chiba, Japan.

Iwan, W. D., Moser, M. A., & Peng, C.-Y. (1985). Some observations on strong-motion earthquake measurement using a digital accelerograph. *Bulletin of the Seismological Society of America*, *75*, 1225–1246.

Jarvis, A., Reuter, H. I., Nelson, A., Guevara, E. (2008). Hole-filled SRTM for the globe version 4, available from the CGIAR-CSI SRTM 90m Database (https://srtm.csi.cgiar.org)

Kanamori, H. (1972). Determination of effective tectonic stress associated with earthquake faulting. The Tottori earthquake of 1943. *Physics of the Earth and Planetary Interiors*, *5*, 426–434. https://doi.org/10.1016/0031-9201(72)90114-8

King, G., Stein, R., & Lin, J. (1994). Static stress changes and the triggering of earthquakes. *Bulletin of the Seismological Society of America*, *84*, 935–993.

Kubo, H., Suzuki, W., Aoi, S., & Sekiguchi, H. (2017). Source rupture process of the 2016 central Tottori, Japan, earthquake (M_{JMA} 6.6) inferred from strong motion waveforms. *Earth, Planets and Space*, *69*(1). https://doi.org/10.1186/s40623-017-0714-3

Lindsey, E. O., & Fialko, Y. (2013). Geodetic slip rates in the southern San Andreas Fault system: Effects of elastic heterogeneity and fault geometry. *Journal of Geophysical Research: Solid Earth*, *118*, 689–697. https://doi.org/10.1029/2012JB009358

Marone, C. J., Scholtz, C. H., & Bilham, R. (1991). On the mechanics of earthquake afterslip. *Journal of Geophysical Research*, *96*(B5), 8441–8452. https://doi.org/10.1029/91JB00275

Matsu'ura, M., & Hasegawa, Y. (1987). A maximum likelihood approach to nonlinear inversion under constraints. *Physics of the Earth and Planetary Interiors*, *47*, 179–187. https://doi.org/10.1016/0031-9201(87)90076-8

Miyazaki, S., Segall, P., Fukuda, J., & Kato, T. (2004). Space time distribution of afterslip following the 2003 Tokachi-oki earthquake: Implications for variations in fault zone frictional properties. *Geophysical Research Letters*, *31*, L06623. https://doi.org/10.1029/2003GL019410

National Research Institute for Earth Science and Disaster Resilience (2016). http://www.fnet.bosai.go.jp/event/tdmt.php?_id=20161021050600&LANG=en

Nishimura, T. (2009). Slip distribution of the 1973 Nemuro-oki earthquake estimated from the re-examined geodetic data. *Earth, Planets and Space*, *61*(11), 1203–1214. https://doi.org/10.1186/BF03352973

Nishimura, T., & Takada, Y. (2017). San-in shear zone in southwest Japan, revealed by GNSS observations. *Earth, Planets and Space*, *69*(1). https://doi.org/10.1186/s40623-017-0673-8

Ohmi, S., Watanabe, K., Shibutani, T., Hirano, N., & Nakao, S. (2002). The 200 Western Tottori Earthquake—Seismic activity revealed by regional seismic networks. *Earth, Planets and Space*, *54*(8), 819–830. https://doi.org/10.1186/BF03352075

Ohta, Y., Miura, S., Iinuma, T., Tachibana, K., Matsushima, T., Takahashi, H., et al. (2008). Coseismic and postseismic deformation related to the 2007 Chuetsu-oki, Niigata Earthquake. *Earth, Planets and Space*, *60*(11), 1081–1086. https://doi.org/10.1186/BF03353140

Oike, K. (1987). *M*6.2 earthquake on October 31, 1983 in the central part of Tottori Prefecture. *Proceedings of Earthquake Prediction Research Symposium*, 87–99, [in Japanese].

Okada, Y. (1992). Internal deformation due to shear and tensile faults in a half-space. *Bulletin of the Seismological Society of America*, *82*(2), 1018–1040.

Okada, Y. (1985). Surface deformation due to shear and tensile faults in a half-space. *Bulletin of the Seismological Society of America*, *75*, 1135–1154.

Research Group for Active Faults of Japan (1991). *Active faults in Japan: Sheet maps and inventories*. Revised Edition. Tokyo: University of Tokyo Press. [in Japanese]

Ross, Z., Kanamori, H., Hauksson, E., & Aso, N. (2018). Dissipative intraplate faulting during the 2016 M_w 6.2 Tottori, Japan earthquake. *Journal of Geophysical Research: Solid Earth*, *123*, 1631–1642. https://doi.org/10.1002/2017JB015077

Sagiya, T. (2004). A decade of GEONET: 1994–2003—The continuous GPS observation in Japan and its impact on earthquakes studies. *Earth, Planets and Space*, *56*(8), 29–41. https://doi.org/10.1186/BF03353077

Sagiya, T., Nishimura, T., Hatanaka, Y., Fukuyama, E., & Ellsworth, W. (2002). Crustal movements associated with the 2000 Western Tottori Earthquake and its fault models. *Jishin*, *2*, 523–534. [in Japanese]

Shen, Z.-K., Jackson, D. D., & Ge, B. X. (1996). Crustal deformation across and beyond the Los Angeles basin from geodetic measurements. *Journal of Geophysical Research*, *101*(B12), 27,957–27,980. https://doi.org/10.1029/96JB02544

Usami, T. (1996). *Materials for comprehensive list of destructive earthquakes in Japan, 416–1995* [Revised and Enlarged Edition] (p. 493). Tokyo, Japan: University of Tokyo Press. Tokyo [in Japanese]

Wdowinski, S., Bock, Y., Zhang, J., Fang, P., & Genrich, J. (1997). Southern California Permanent GPS Geodetic Array: Spatial filtering of daily positions for estimating coseismic and postseismic displacements induced by the 1992 Landers earthquake. *Journal of Geophysical Research*, *102*(B8), 18,057–18,070.

Wessel, P., & Smith, W. H. F. (1998). New, improved version of the Generic Mapping Tools released. *Eos, Transactions American Geophysical Union*, *79*(47), 579. https://doi.org/10.1029/98EO00426

Zumberge, J. F., Heflin, M. B., Jefferson, D. C., & Watkins, M. M. (1997). Precise point positioning for the efficient and robust analysis of GPS data from large networks. *Journal of Geophysical Research*, *102*(B3), 5005–5017. https://doi.org/10.1029/96JB03860